In-situ growth of ZIF-8 nanocrystals on biochar for boron adsorption

Mina Luo [a,b,*], Chunmei Zhu [a], Qingmei Chen [c], Fang Song [d], Weiduo Hao [e], Zhengtao Shen [f], Kurt O. Konhauser [e], Daniel S. Alessi [e], Cheng Zhong [g,**]

[a] *College of Chemistry and Chemical Engineering, Southwest Petroleum University, Chengdu, Sichuan 610500, China*
[b] *Oil & Gas Field Applied Chemistry Key Laboratory of Sichuan Province, Chengdu, Sichuan 610500, China*
[c] *Research Institute of Natural Gas Technology, PetroChina Southwest Oil & Gasfield Company, Sichuan 610213, China*
[d] *Chengdu Xiyouhuawei Science & Technology Co, Ltd., Sichuan 610500, China*
[e] *Department of Earth and Atmospheric Sciences, University of Alberta, Edmonton, Alberta T6G 2E3, Canada*
[f] *School of Earth Sciences and Engineering, Nanjing University, Nanjing, Jiangsu 210023, China*
[g] *Department of Ocean Science, The Hong Kong University of Science and Technology, Hong Kong, China*

HIGHLIGHTS

- Biochar (BC) template mitigates ZIF-8 agglomeration.
- BC/ZIF-8 exhibits excellent adsorption properties for boron.
- BC/ZIF-8 has excellent reusable capacity for boron.
- Hydrogen bonding and electrostatic attraction have critical roles in boron bonding to BC/ZIF-8.

GRAPHICAL ABSTRACT
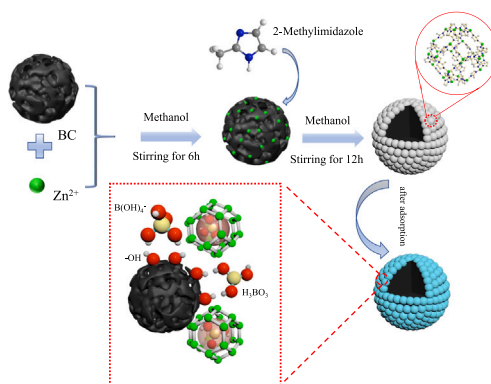
ARTICLE INFO

ABSTRACT

Removing boron (B) from aqueous solution is economically and environmentally important in the treatment of many industrial and agricultural wastewater streams. Here, we produced canola straw-derived biochar (BC), a low-cost and green adsorbent, as a template to prepare a BC/ZIF-8 (zeolite-like imidazolate framework) composite material. We then performed a series of batch experiments and material characterization to evaluate the adsorption processes and practical applications of the material. The results showed that the maximum adsorption capacity of BC/ZIF-8 for B from a low total dissolved solids (TDS) aqueous solution was 44 mg g^{-1} (adsorbent dosage is 0.5 g L^{-1}, pH=6, C_0 =300 mg L^{-1}). Compared to ZIF-8 alone, the adsorption capacity of B to BC/ZIF-8 increased by 76%. In the adsorption tests conducted in the low TDS solution, the adsorption process was well-represented using a pseudo-first-order kinetics model and the Langmuir adsorption isotherm. Through six regeneration cycles, we demonstrated that BC/ZIF-8 remains a robust sorbent for B. Hydraulic fracturing (HF), a

---

* Corresponding author at: College of Chemistry and Chemical Engineering, Southwest Petroleum University, Chengdu, Sichuan 610500, China.
** Corresponding author.
E-mail addresses: mnluo@swpu.edu.cn (M. Luo), chengzhong@ust.hk (C. Zhong).

key technology for oil and gas stimulation, produces a large amount of flowback and produced water (FPW). BC/ZIF-8 was used to remove boron from FPW, achieving a maximum adsorption capacity of 15.45 mg g^{-1} (C$_0$ =42 mg L^{-1}), 5.99% lower than that of pure B solution with similar conditions. Physicochemical characterization of BC/ZIF-8 showed that it has a stable structure and suggested that B adsorption to BC/ZIF-8 was primarily due to hydrogen bonding and electrostatic attraction between B(OH)$_4^-$ and the positively charged BC/ZIF-8 at pH < PZC. Our study shows that BC-based metal-organic frameworks (MOFs) have the potential for broader industrial applications and water treatment.

1. Introduction

Hydraulic fracturing (HF) is a key technology that injects a large volume of water into a low-permeability reservoir to create fractures to enhance the natural gas and oil yield. HF combined with horizontal drilling is a widely used and efficient technology for unconventional oil and gas extraction [1]. However, flowback and produced water (FPW), a by-product during the HF process, may cause adverse effects on aquatic organisms in the event of fluid releases at the surface [2–5]. FPW comprises inorganic elements released by the interaction between HF fluid and the formation rocks as well as organic contaminants (e.g., polycyclic aromatic hydrocarbons and other organic compounds) from both hydrocarbons and HF fluid chemical additives [6–8]. B is a critical element in HF process and in FPW, which is present in HF in the form of a B cross-linking agent guar gum [9]. However, residual B in the FPW may be a potential pollutant in the event of a spill and it also leads to undesirable crosslinks of guar gum or macromolecules during operations [10–12], impeding the reuse of the FPW for subsequent HF operations,

Reported methods for removing B in solution include chemical precipitation [13], ion exchange [14], reverse osmosis [15], and adsorption [8]. Adsorption could be a cost-effective method of recovering B, particularly if the adsorbent can be recycled. The B adsorption capacity of various adsorbents has been investigated, including natural polysaccharides [16–18], carbon aerogels [19], nanomaterials [20,21], metal oxides [22], layered double hydroxides [23], and membrane materials [24]. Among them, metal-organic framework materials (MOFs) have the advantages of both organic and inorganic adsorbents because they are self-assembled by metal ions/clusters and organic ligands [25–27]. Meanwhile, the porosity of MOFs is often greater than other adsorbents and can be controlled by changing the manufacturing conditions [28]. Particularly, a MOF with a zeolite-like imidazolate framework (ZIF-8) is widely used in photocatalysis, gas separation, and adsorption [29–31], which is prepared by using Zn(II) as the metal node and 2-methylimidazole as the organic ligand [32,33]. ZIF-8 has been shown as an ideal adsorbent for treatment of aqueous trace elemental contamination due to its desirable physical and chemical properties, such as high crystallinity, elevated porosity, large specific surface area, and excellent hydrothermal stability in water [34–36]. However, ZIF-8 nanoparticles are prepared using traditional synthetic methods, which often leads to particle agglomerate that can reduce the number of available adsorption sites [37,38].

Graphene oxide (GO) [39], SiO$_2$ [40], and films [41] have been combined with ZIF-8 to mitigate the agglomeration of ZIF-8. This effect is attributed to metal coordination between the abundant oxygen-containing groups on the surfaces of these materials with the metal centers of ZIF-8 [42]. However, GO and SiO$_2$ are expensive and the latter is harmful to health, and films preparation process is complicated. Biochar (BC) produced at modest pyrolysis temperatures has an aromatic surface that contains a variety of oxygen-containing functional groups (e.g., -COOH, -OH, -CHO) [43–47]. Indeed, the abundant functional groups and high specific surface area of BC may also be capable of mitigating ZIF-8 agglomeration. Besides, the dissociation of oxygen-containing functional groups and negatively charged surface may facilitate the distribution of Zn(II) on the surface of BC [48]. In addition, the raw materials of biochar come from a wide range of low-cost sources (including agricultural waste and municipal sludge), so

using BC can benefit waste management [49]. Currently, few reports have been reported using BC to mitigate ZIF-8 agglomeration.

In this study, we used BC as a carrier for ZIF-8 to develop a BC/ZIF-8 MOF composite material and investigated its B adsorption capacity in FPW. We conducted several cycles of B adsorption and regeneration, and then characterized the physiochemical properties of BC/ZIF-8 before and after adsorption to understand the specific mechanisms underpinning B adsorption. Ultimately, we aim to develop a new material to recover B from a variety of wastewater streams that has broad industrial applications.

2. Materials and methods

2.1. Workflow and materials

We developed BC/ZIF-8 using an in-situ growth method and implemented an integrated approach to investigate BC/ZIF-8-B interactions (Fig. 1). Zinc nitrate hexahydrate (Zn(NO$_3$)$_2$6H$_2$O), 2-methylimidazole, methanol, ethanol, boric acid, hydrochloric acid (HCl), and sodium hydroxide (NaOH) were purchased from Chron Chemicals Inc (Chengdu, China). All chemicals used in the experiments were of analytical grade (AR). A canola straw BC was prepared using an in-house method (Supplementary Information). We prepared ZIF-8 nanocrystals by referring to the previously reported synthesis method of ZIF-8 [37] and loaded them on BC; 0.774 g Zn (NO$_3$)$_2$6H$_2$O and 0.21 g BC were dissolved in 60 mL methanol and stirred slowly for 6 h. Then, 0.789 g 2-methylimidazole was dissolved in 60 mL methanol and mixed with the Zn (NO$_3$)$_2$6H$_2$O-BC solution. After stirring the resulting solution for 12 h, the product was washed with methanol and subsequently dried at 70 °C for 12 h to obtain the BC/ZIF-8 composite material.

2.2. Characterization of BC/ZIF-8

2.2.1. X-ray diffraction

An X-ray diffractometer (X'Pert PRO MPD, PANalytical B.V., Netherlands) was used to characterize the crystal structure of BC/ZIF-8 composites. The sample was placed on a glass slide and kept at the same level as the working surface (Cuλ=0.154 nm), using Cu Kα radiation, an accelerating voltage and a current of 40 kV and 40 Ma, respectively. A scanning step size of 0.0167°/step, a dwell time of 12 s, a rate of 0.1°/min, and measurements were conducted between 2θ values of 5–70°. X-ray analysis and other experiments were all done at Southwest Petroleum University in China.

2.2.2. FTIR spectroscopy

To determine the near surface bonds of the BC/ZIF-8 composite material, we used a Nicolet 6700 Fourier Transform Infrared Spectrometer (Thermo Scientific, USA) to determine changes in functional groups of the adsorbents. The samples were uniformly ground with dry KBr at a ratio of 1:200 and were pressed into the disc at a pressure of 10 MPa for 1 min

2.2.3. TGA and DTG analysis

A TGA/DSC 3 + (Mettler, Switzerland) instrument was used to conduct the Thermo Gravimetric Analysis (TGA) to investigate the thermal stability of adsorbents. The Derivative Thermogravimetric

(DTG) analysis curve was obtained by the first derivative of the TGA curve with respect to temperature (or time). With N_2 as the protective gas, the heating rate was 10 °C/min and the temperature range was from 30° to 800°C.

2.2.4. Scanning electron microscope (SEM) analysis

A Hitachi Regulus 8100 Scanning Electron Microscopy (Hitachi, Japan) was used to image changes in the morphology of adsorbents. The sample was attached to conductive tape and coated with gold prior to SEM analysis.

2.2.5. Surface area and porosity analysis

The specific surface area and pore size distribution of BC/ZIF-8 were measured using an automatic specific surface and ASAP2460 porosity analyzer (Micromeritics Instrument Corp, USA) using BET analysis. The N_2 adsorption isotherms of the three samples were measured at 77 K. The samples were degassed under vacuum at 150 °C for 8 h.

2.2.6. XPS analysis

A K-Alpha X-ray Photoelectron Spectrometer (XPS) (Thermo Scientific, USA) was used to analyze the elemental composition and valence state of the surfaces of the adsorbents. Monochromatic Al Kα (1486.8 eV) radiation was used as the excitation spectrum, the test tube voltage was 15Kv, and the test tube current was 10 mA during XPS measurements.

2.2.7. Zeta potential measurement

Zeta potential was measured by the phase analysis light scattering method with Zeta PALS 190 Plus (Brookhaven, USA). Charged particles move under the action of an applied electric field, and the movement of the charge causes the scattered light to shift in frequency (Doppler shift). Using the spectral drift analysis technology, the electrophoretic mobility of the particles is obtained, and the Zeta potential is calculated using Henry's equation [50] (Eq. 1).

$$U_e = 2\varepsilon z f(\kappa a)/3\eta \tag{1}$$

where U_e is the electrophoretic mobility; ε is the dielectric constant; η is the absolute zero shear viscosity of the medium; $f(\kappa a)$ is the Henry function; and κa is a measure of the ratio of the particle radius to the Debye length.

2.2.8. Particle size analysis

The particle sizes of BC and BC/ZIF-8 were measured by a Laser Light Scattering System BI-200SM (Brookhaven, USA). The size of BC and BC/ZIF-8 was measured by static light scattering at the temperature of 25 ℃, pressure of 0.1 MPa, laser intensity of 150–500 kcps, and wavelength of 535 nm.

2.3. Batch experiments of B adsorption on BC/ZIF-8

A B stock solution of 1000 mg L^{-1} was prepared from boric acid and deionized water. The concentrations used in subsequent experiments were all obtained by diluting the B stock solution. After adsorption reached equilibrium, the supernatant was filtered through a 0.22 μm nylon membrane.

The equilibrium adsorption capacity (Q_e) and removal rate (% removal) of B was calculated by Eqs. (2) and (3):

$$Q_e = (C_0 - C_e)V/m \tag{2}$$

$$\% \text{ Removal} = (C_0 - C_e) \times 100/C_0 \tag{3}$$

Where C_0 (mg L^{-1}) refers to the initial B concentration; C_e (mg L^{-1}) is the B concentration after equilibrium adsorption of B on BC/ZIF-8; V (mL) is the volume of B solution; m (g) is the mass of adsorbent.

2.3.1. Boron adsorption as a function of adsorbent concentration

The B adsorption behavior was studied as a function of different adsorbent concentrations (0.2, 0.5, 1, 2, 3, 5, 8 g L^{-1}). The initial concentration of B was 300 mg L^{-1}, the initial pH was 6, the adsorption time was 24 h and the adsorption temperature was 298 K (~25 °C).

2.3.2. Boron adsorption as a function of solution pH

The pH edge of B adsorption onto BC/ZIF-8 was performed over a pH range of 3–11. The solution pH was adjusted by adding small aliquots of 1 M hydrochloric acid and 1 M sodium hydroxide. The pH edge was performed at an adsorbent concentration of 0.5 g L^{-1} and an initial B concentration of 300 mg L^{-1} at room temperature (~25 °C). After 24 h of adsorption, samples were collected for B analysis.

2.3.3. Boron adsorption kinetics

The adsorption kinetics experiments were performed at room tem-

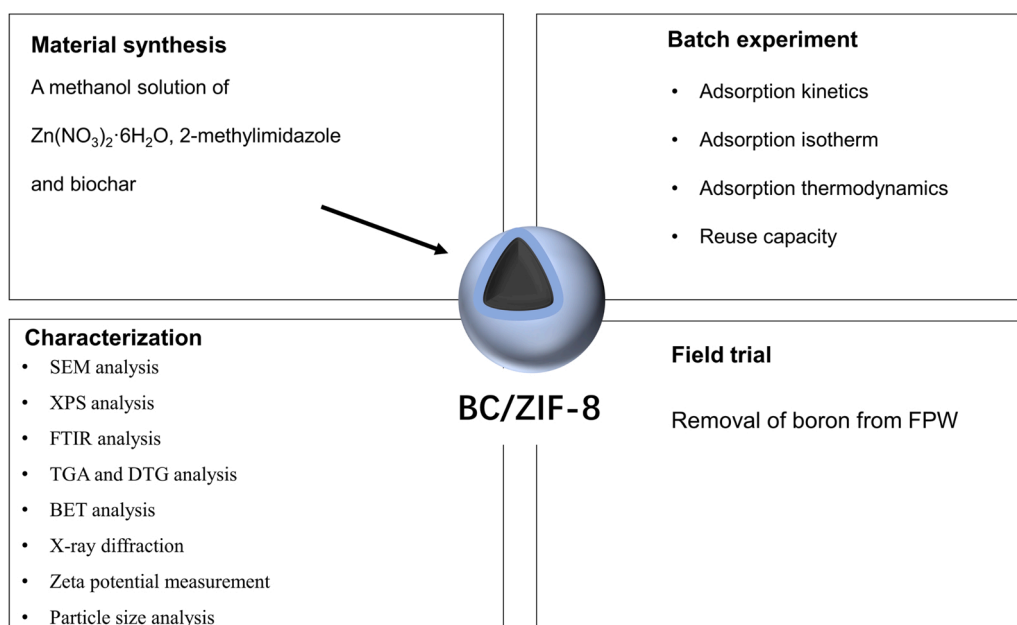| Material synthesis	Batch experiment
A methanol solution of Zn(NO$_3$)$_2$·6H$_2$O, 2-methylimidazole and biochar	• Adsorption kinetics • Adsorption isotherm • Adsorption thermodynamics • Reuse capacity
Characterization	Field trial
• SEM analysis • XPS analysis • FTIR analysis • TGA and DTG analysis • BET analysis • X-ray diffraction • Zeta potential measurement • Particle size analysis	Removal of boron from FPW

BC/ZIF-8

Fig. 1. Experimental design of this study, including material synthesis, material characterization, batch adsorption experiments, and field trial.

perature (~25 °C) at an initial B concentration of 300 mg L^{-1} and an adsorbent concentration of 0.5 g L^{-1}. The pH of the kinetics experiments was fixed at 6, and samples were collected for B analysis after 1, 4, 9, 19, 34, 54, 94, 154, 244, 364, 604, and 1440 min of reaction respectively. The pseudo-first-order kinetic model (Eq. 4) and pseudo-second-order kinetic model (Eq. 5) are mathematical models used to describe adsorption kinetics.

$$Q_t = Q_e\left(1 - e^{-k_1 t}\right) \tag{4}$$

$$Q_t = k_2 Q_e^2 t / (1 + k_2 Q_e t) \tag{5}$$

Where Q_e (mg g^{-1}) is the equilibrium adsorption capacity of BC/ZIF-8 for B; Q_t (mg g^{-1}) is the adsorption capacity at any time; k_1 (min^{-1}) is the pseudo-first-order equilibrium rate constant; k_2 (g mg^{-1} min^{-1}) is the pseudo-second-order equilibrium rate constant. These two models were applied to model the adsorption kinetics data.

2.3.4. Boron adsorption isotherm

Boron adsorption as a function of initial B concentrations (40, 80, 100, 200, 300, 400, and 800 mg L^{-1}) were performed at 298 K (~25 °C) for 24 h. The adsorbent concentration was 0.5 g L^{-1}, and the pH of the adsorption process was fixed at 6. The Langmuir isotherm model (Eq. 6) and the Freundlich isotherm model (Eq. 7) were used to fit the data using the following equations:

$$Q_e = Q_m K_L C_e / (1 + K_L C_e) \tag{6}$$

$$Q_e = K_F C_e^{\frac{1}{n_F}} \tag{7}$$

Where Q_m (mg g^{-1}) is the maximum adsorption capacity of the monolayer; Q_e (mg g^{-1}) is the equilibrium adsorption capacity of BC/ZIF-8 for B; C_e (mg L^{-1}) is the B concentration after equilibrium adsorption of B on BC/ZIF-8; K_L is the Langmuir constant; K_F is the Freundlich constant for the adsorption capacity; $1/nF$ is the Freundlich constant for the adsorption strength.

2.3.5. Boron adsorption as a function of temperature

Boron adsorption onto BC/ZIF-8 was investigated at 298 K (~25 °C), 308 K (~35 °C), and 318 K (~45 °C). At each adsorption temperature, the adsorption condition was the same as for the adsorption isotherm experiments described above, where the initial concentrations of B were 40, 80, 100, 200, 300, 400, and 800 mg L^{-1}, the adsorption pH was 6, and the adsorption time was 24 h. The Gibbs free energy (ΔG), enthalpy (ΔH), and entropy (ΔS) were calculated by Eq. (6) and Eq. (7).

$$ln K_P = \Delta S/R - \Delta H/RT \tag{6}$$

$$\Delta G = \Delta H - T\Delta S \tag{7}$$

Where K_P is the distribution constant; R is the gas constant (8.314 J mol^{-1} K^{-1}); T(K) is the temperature.

2.4. Reuse capacity

The regeneration performance of BC/ZIF-8 was investigated through 6 cycles of experiments. The B-loaded BC/ZIF-8 (BC/ZIF-8-B) and 0.5 M NaOH/ethanol solution were added to the conical flask at a mass ratio of 1:20. After shaking for 12 h at 160 rpm at room temperature, the BC/ZIF-8-B was washed three times with ethanol and was dried at 343 K (~70 °C) for 12 h to obtain a regenerated adsorbent. During these experiments, the pH was 6, the initial B concentration was 300 mg L^{-1}, the temperature was 298 K (~25 °C), the oscillation frequency was 160 rpm and the adsorption time was 24 h.

2.5. Boron recovery from FPW

To investigate the B removal capacity from FPW by BC/ZIF-8, we collected FPW from a wastewater storage pond from a shale gas well in Southwest China in July 2021. Before conducting the adsorption experiments and elemental profiling, the insoluble particles were removed by passing the fluid through 0.22 μm membranes. The elemental concentrations of sodium (Na), potassium (K), calcium (Ca) and magnesium (Mg) cations in HF-FPW were measured using atomic absorption spectroscopy (AAS) (East & West Analytical Instruments, Beijing, China). Sulfate was determined by barium chromate spectrophotometry (INESA, Shanghai, China), and the concentration of dissolved inorganic carbon was determined by titration. For adsorption experiments, we used both FPW and a control group comprised of B in deionized water (B concentrations were prepared to be the same as the FPW). To conduct an adsorption experiment, 10 mg of BC/ZIF-8 was suspended in 20 mL of the FPW and or the control group solution. The adsorption pH was set to 6, experiments were conducted at room temperature, and samples were filtered for analysis after 24 h.

3. Results and discussion

3.1. Characterization of BC/ZIF-8

As shown in Fig. 2a, XRD results show that peaks of graphene layer stacking (002) with an ordered hexagonal structure (100) appeared in the XRD pattern of BC, indicating that BC has a graphitized structure [51–54]. No difference was observed between the spectra of synthesized ZIF-8 and the standard ZIF-8, indicating that there is no crystal structure change during ZIF-8 synthesis. The corresponding peaks are 7.334°, 10.379°, 12.72°, 18.026°, and 26.665°, corresponding to (011), (002), (112), (222), (015) on the simulated ZIF-8 [37], respectively. The peaks in the XRD pattern of the synthesized ZIF-8 were sharp, indicating that the synthesized ZIF-8 is well-ordered. There is very little difference between the XRD spectra of BC/ZIF-8 and ZIF-8 indicating that ZIF-8 grew tightly and uniformly on BC, and BC has no significant effect on the crystallization of ZIF-8. The XRD patterns of BC/ZIF-8-B and BC/ZIF-8 on the XRD patterns are similar, which indicates the crystallinity of the BC/ZIF-8 was stable during the adsorption process. As shown in Figs. 2b, 2c and 2d, compared with ZIF-8, all the diffraction peaks of BC/ZIF-8 are shifted to the left, indicating that ZIF-8 is successfully loaded on BC. In addition, all the diffraction peaks of BC/ZIF-8-B are shifted to the right compared with ZIF-8. The overall shift of the diffraction peak is attributed to the change of the crystal plane spacing caused by the introduction of other substances into the ZIF-8 [55]. The stable structure is promising for the repeated reuse of BC/ZIF-8 in field wastewater treatment operations.

Changes in the apparent morphologies of the materials during the adsorption process were observed by SEM and are summarized in Fig. 3. The SEM images show ZIF-8 was loaded on BC without profound agglomeration. The average particle size of ZIF-8 is about 31.9 nm and the average particle size of ZIF-8 in BC/ZIF-8 is about 132.9 nm (Fig. 4). The cause of the ZIF-8 particle size increase is electrostatic interaction [56]. The negatively charged BC, as the carrier of ZIF-8, has electrostatic attraction with Zn^{2+}, which allows ZIF-8 to grow on its surface. Meanwhile, the structure of BC/ZIF-8 is stable after B adsorption, which is also consistent with the XRD analysis. Fig. 3d shows that C, N, O, Zn and B appear in BC/ZIF-8-B, indicating a uniform adsorption process. The percentage of C, N, O, and Zn in BC/ZIF-8 are shown in Table 1. By theoretical calculation (Supplementary Information), the proportions of ZIF-8 and BC in BC/ZIF-8 were 38.3% and 61.7%, respectively.

We analyzed TGA and DTG (Fig. 5) to compare the thermal stability of BC/ZIF-8 and ZIF-8. The first stage of weight loss of ZIF-8 was below 479 °C with T$_{max}$ peak at 306 °C, which was primarily due to the loss of bound water, and that for BC/ZIF-8 was below 347 °C with T$_{max}$ peak at 246.5 °C primarily due to the loss of bound water and hemicellulos [57].
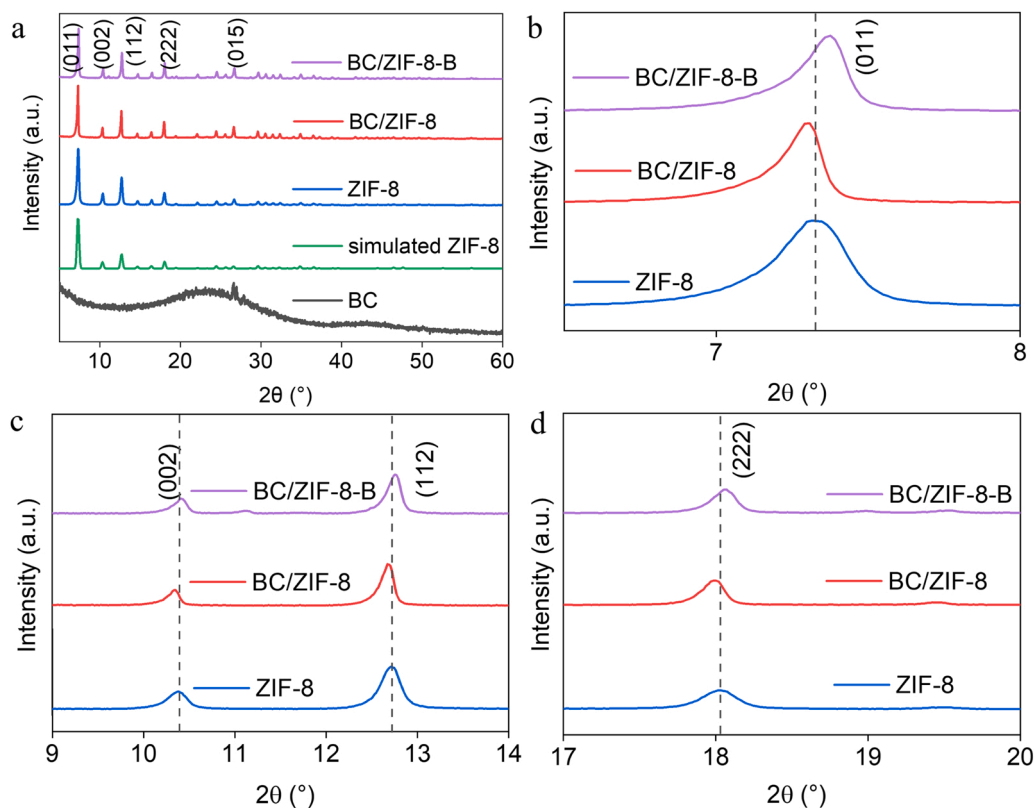
Fig. 2. (a) X-ray diffraction patterns of BC, ZIF-8, BC/ZIF-8, simulated ZIF-8 and BC/ZIF-8-B; the diffraction peak of ZIF-8 shifted after adding BC with (b) 2θ < 8°, (c) 2θ = 9–14°, (d) 2θ = 17–20°.
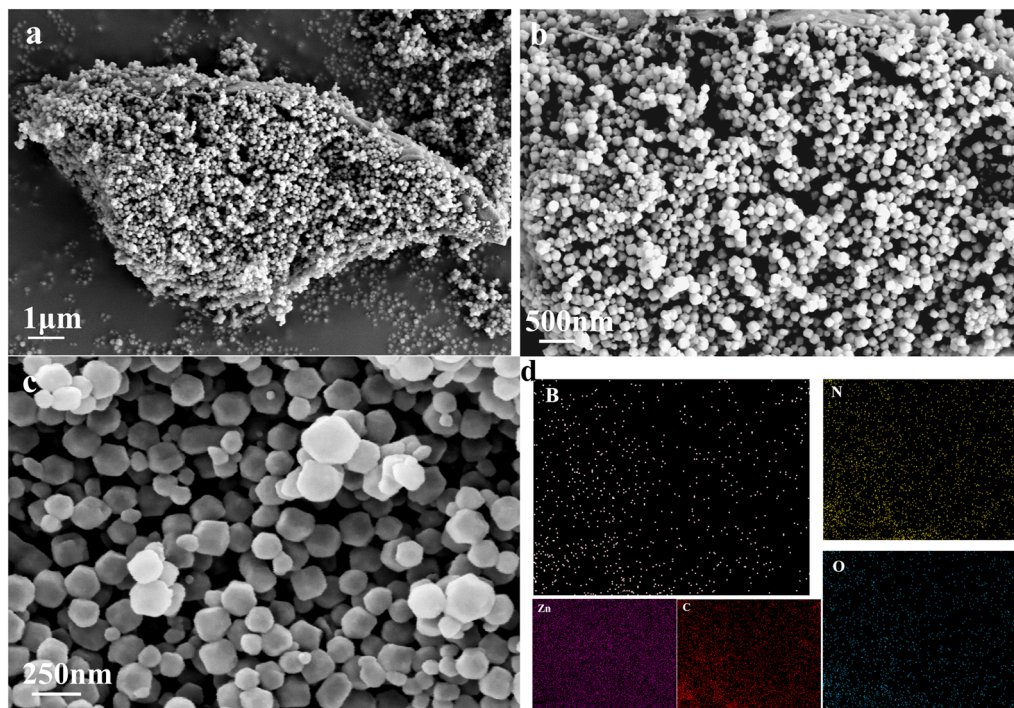

Fig. 3. SEM images for the comparison of surface morphologies of BC/ZIF-8, and BC/ZIF-8-B, (a) (b) SEM image of BC/ZIF-8, (c) SEM image of BC/ZIF-8-B, (d) The elemental mapping of C, N, O, Zn and B on BC/ZIF-8-B nanoparticles.

The second stage of weight loss of ZIF-8 was between 479 °C and 700 °C with T_{max} peak at 586 °C. The weight loss of ZIF-8 in this stage was mainly caused by the cleavage of coordination bonds of metal nodes Zn (II) and the decomposition of organic ligands[58]. In comparison, the second stage of weight loss of BC/ZIF-8 was between 347 °C and 655 °C with T_{max} peak at 516 °C, which was mainly caused by the
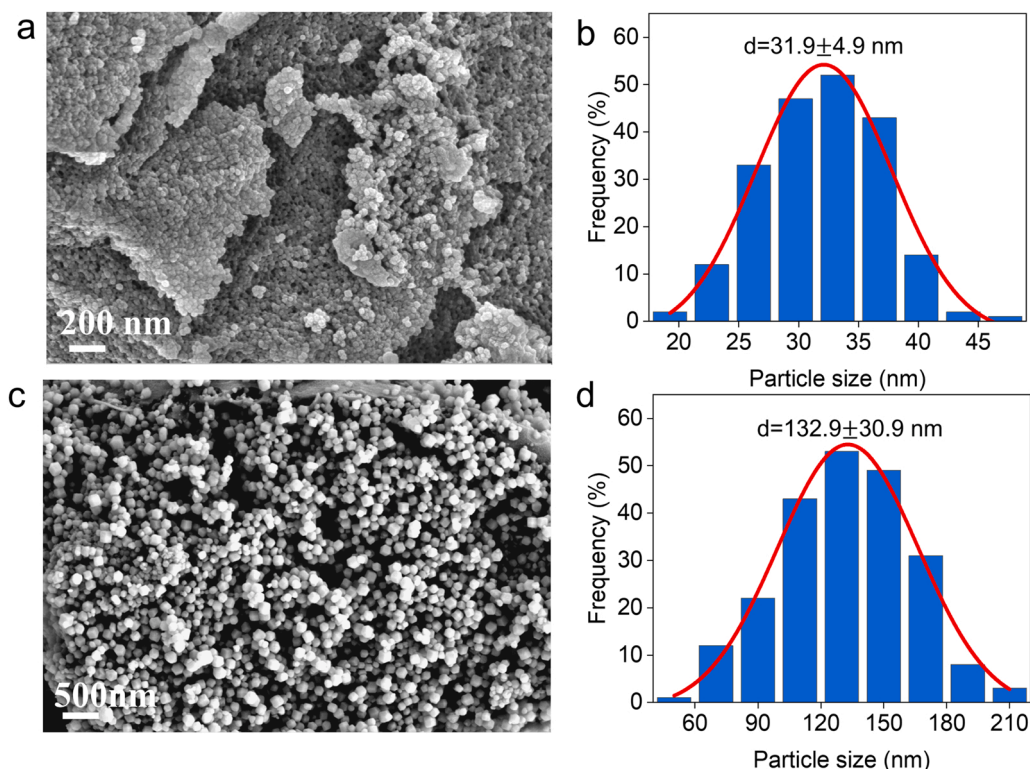
Fig. 4. SEM images (a) and particle size distribution (b) of ZIF-8; SEM images (c) and Particle Size Distribution (d) of BC/ZIF-8.

Table 1
Elemental composition of BC/ZIF-8.

Elements	Wt%
C	71.43
N	10.84
O	6.82
Zn	10.91

decomposition of ZIF-8 components and the cellulose and lignin of BC [57,59]. The third stage of weight loss of ZIF-8 was above 700 °C with T_{max} peak at 772 °C and of BC/ZIF-8 was above 740 °C, which involves the combustion of BC and the thermal decomposition of ZIF-8 [60]. Both materials lost 47% in all three stages. These results indicate that the synthesized BC/ZIF-8 has good thermal stability.

The BET surface area results of BC, ZIF-8 and BC/ZIF-8 are given in Fig. 6. Type IV adsorption-desorption isotherms were used to accurately model adsorption to the mesoporous structure of the materials [61,62]. The specific surface area of canola straw BC was 14.12 m² g⁻¹, which is consistent with canola straw BC surface areas previously reported [63]. The specific surface areas of ZIF-8 and BC/ZIF-8 were 1317.74 m² g⁻¹ and 729.16 m² g⁻¹, respectively. However, the adsorption capacity of BC/ZIF-8 is larger than that of ZIF-8 (Fig. 8a), which may be due to the enhanced interaction of boron and adsorbate by nanostructure hybridization [38]. The BET analysis (Fig. 6b) showed that the pore size of ZIF-8 is not homogenously distributed and pores of approximately 200 Å are dominant in ZIF-8. By comparison, the pore size of the BC/ZIF-8 is more homogenously distributed and pores at 200 Å are substantially reduced during modification. The fraction of pores with 20–40 Å in BC/ZIF-8 increased and are higher than that in ZIF-8, indicating modification generated some relatively small pores compared to that in ZIF-8 (Fig. 6b, inset plot). For BC/ZIF-8, this result may indicate that some large macromolecular species may be blocked by the pores of BC/ZIF-8, resulting in higher selectivity for B. The particle sizes of BC and BC/ZIF-8 are shown in Figs. 6c and 6d. The particle size test results of BC show that there is an absorption peak at 4024.9 nm, which indicates that the average particle size of BC is 4024.9 nm. The absorption peak of BC/ZIF-8 appears at 7103.9 nm, suggesting that the average particle size
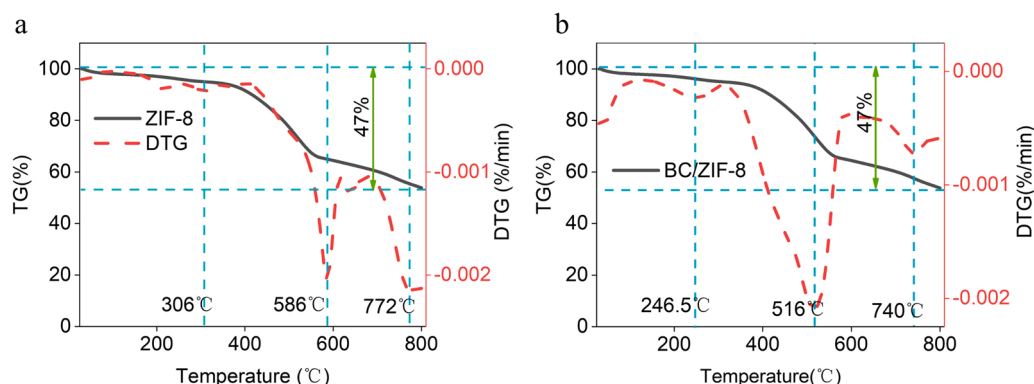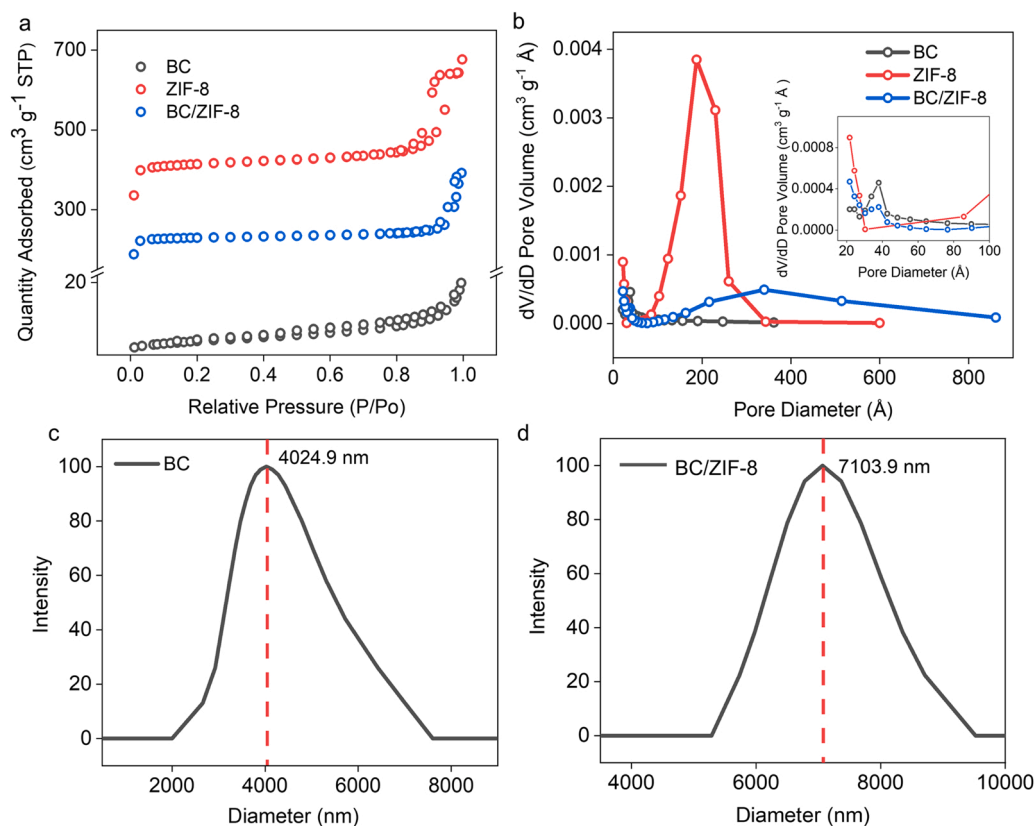

Fig. 5. TG-DTA curves of (a) ZIF-8 and (b) BC/ZIF-8.

6

Fig. 6. (a) N$_2$ adsorption-desorption isotherms of BC, ZIF-8 and BC/ZIF-8, (b) pore size distribution of BC, ZIF-8 and BC/ZIF-8, the particle size of BC (c) and BC/ZIF-8 (d).

of BC/ZIF-8 is 7103.9 nm. The larger particle size of BC/ZIF-8 than BC is caused by the growth of ZIF-8 on BC, which is consistent with the results of XRD and SEM characterization.

3.2. Boron adsorption

3.2.1. Adsorbent dosage

Fig. 7a shows the impact of sorbent concentration on B adsorption onto BC/ZIF-8. While increasing adsorbent dosage resulted in an increased B removal rate, it decreased the equilibrium adsorption capacity (Qe). For example, at an adsorbent concentration of 8 g L^{-1}, BC/ZIF-8 had an 11% improvement in removal rate but had a Qe that was 78 mg g^{-1} lower than at an adsorbent concentration of 0.2 g L^{-1}. Among them, 0.5 g L^{-1} BC/ZIF-8 had the largest increase in B removal rate and adsorption capacity. Considering the cost, the optimal concentration of the BC/ZIF-8 for B adsorption was around 0.5 g L^{-1}. Increasing the adsorbent concentration increased the overall net specific surface area and adsorption sites, with the overall effect being enhanced B removal from the solution. The low adsorption capacity was probably because increasing adsorbent concentration led to the blocking of adsorption sites due to the particle aggregation [64].

3.2.2. Initial pH

The B adsorption capacity to BC/ZIF-8 initially increased with an increase in pH from 3 to 6, and subsequently decreased as the pH increased to 11 (Fig. 7b). The zeta potential results (as shown in Fig. 7b) show the point of zero charge (PZC) of BC/ZIF-8 is ~9.03, which indicates that the surface of BC/ZIF-8 is positively charged at pH < 9.03 and negatively charged at pH > 9.03. The adsorption capacity reached a maximum at pH = 6, which was 44 mg g^{-1}. Under acidic conditions, reduced pH leads to ZIF-8 dissolution [65]. With an increase in pH (>6), the deprotonation of B aqueous species led to B being more negatively

charged and a lower electrostatic attraction between BC/ZIF-8 and B aqueous species, thus, reducing adsorption capacity.

3.2.3. Adsorption kinetics

The adsorption of B as a function of time is illustrated in Fig. 8a. The adsorption capacity of ZIF-8 and BC/ZIF-8 on B reached a plateau after approximately 300 min. The adsorption capacity of B on BC/ZIF-8 was 44 mg g^{-1}, which was higher than that of ZIF-8 (25 mg g^{-1}). To further explore the kinetics of B adsorption by ZIF-8 and BC/ZIF-8, the pseudo-first-order kinetics model and pseudo-second-order kinetics model were used to fit our adsorption data (the parameters of the B adsorption kinetics models are presented in Table S1). The pseudo-first-order kinetics model better reproduces the experimental data for both ZIF-8 and BC/ZIF-8 adsorption of B. According to previous studies, the adsorption of B by ZIF-8 and BC/ZIF-8 is likely controlled by diffusion [66,67].

3.2.4. Adsorption isotherms

The amount of B adsorption increased with both higher initial concentration of B and adsorption temperature (Fig. 8b). The Langmuir and Freundlich isotherm adsorption model fits are shown in Figs. 8c, 8d, 8e and 8f (for detailed parameters of the models, see Table S2). According to the linear regression coefficient, the Langmuir isotherm model better reproduces the adsorption behavior of B on ZIF-8 and BC/ZIF-8. Based on previous studies, the Langmuir isotherm indicates that B adsorption on ZIF-8 and BC/ZIF-8 was of a monolayer type on a uniform surface [53,68,69].

3.2.5. Adsorption thermodynamics

Negative values of ΔG at all tested temperatures (298 K: −0.588 kJ mol^{-1}, 308 K: −0.682 kJ mol^{-1}, and 318 K: −0.929 kJ mol^{-1}) suggest that the adsorption of B by BC/ZIF-8 was a spontaneous process. ΔH was positive (4.438 kJ mol^{-1}) which indicates that the adsorption of
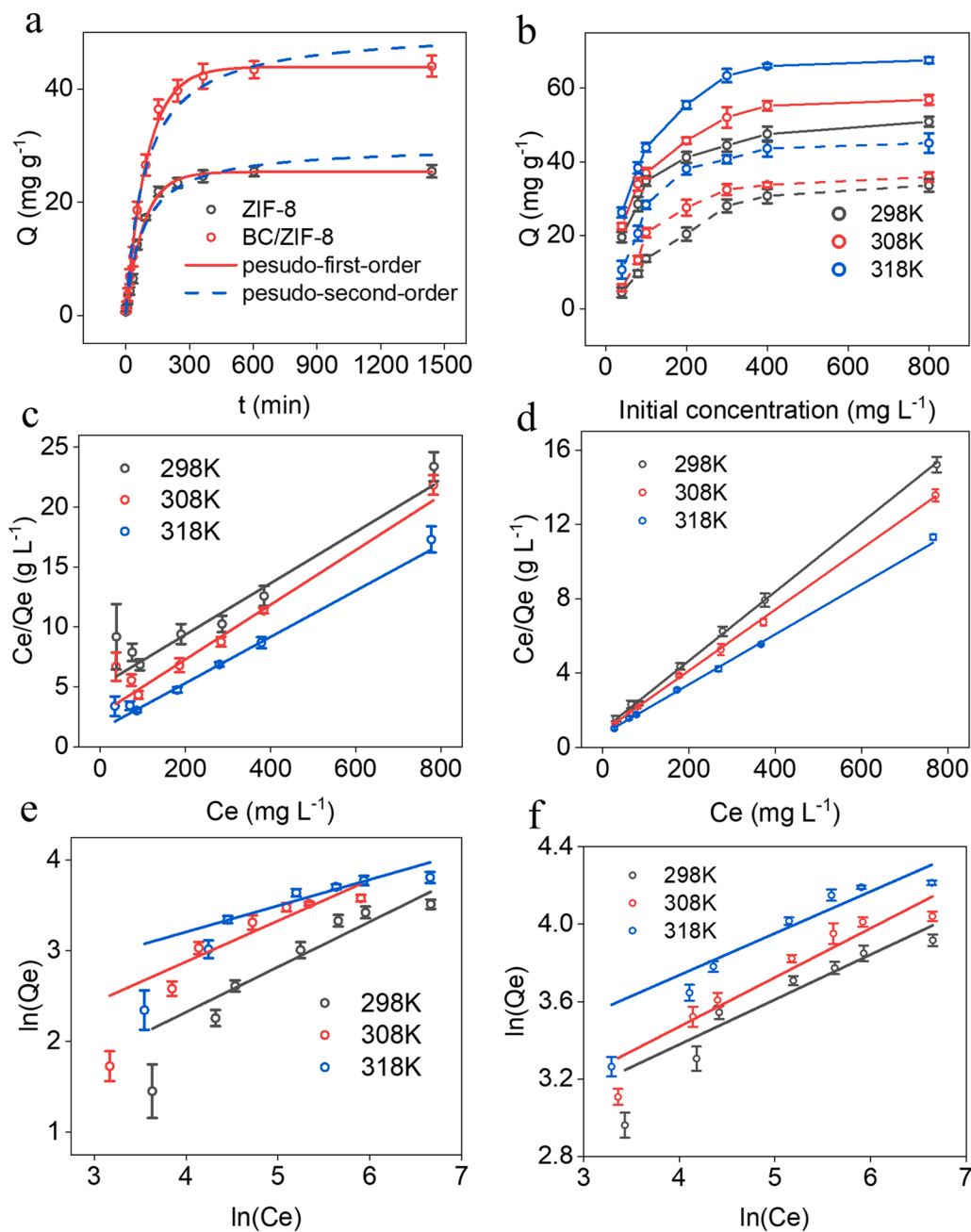
Fig. 8. (a) The adsorption kinetics of B on ZIF-8 and BC/ZIF-8; (b) the adsorption isotherms of B on ZIF-8 (dashed line) and BC/ZIF-8 (solid line); (c) Langmuir curve of B adsorption by ZIF-8; (d) Langmuir curve of B adsorption by BC/ZIF-8; (e) Freundlich curve of B adsorption by ZIF-8; (f) Freundlich curve of B adsorption by BC/ZIF-8. Error bars represent standard deviations (n = 4).

B on BC/ZIF-8 was an endothermic process, while ΔS in positive value (16.867 kJ mol^{-1}) which indicates a good affinity of B onto BC/ZIF-8 [70]. The positive ΔS suggested that dispersion of the adsorbent and the randomness of the solid-liquid interface increased as a function of increasing adsorption temperature [71]. Based on the negative ΔG values and positive ΔH and ΔS values, the adsorption of B on BC/ZIF-8 was mainly driven by the entropy effect [21].

3.3. Cycle testing

The promise of high recyclability of the BC/ZIF-8 material was revealed by performing 6 cycles of B adsorption and desorption (Fig. 9). After the 6th cycle, the equilibrium adsorption capacity decreased by 9.94% from the first adsorption. After 6 cycles of B adsorption onto BC/

ZIF-8, the BC/ZIF-8 had a persistent equilibrium adsorption capacity of 40 mg g^{-1}, displaying 90.06% of the original adsorption capacity. As shown in Fig. 10, the main peak of ZIF-8 remains in the XRD pattern after the 6th adsorption and desorption, which indicates that BC/ZIF-8 has good stability. The surface area of BC/ZIF-8-B decreased to 391.89 m^2 g^{-1} after six sorptions, and the surface area increased slightly to 453.73 m^2 g^{-1} after desorption with NaOH/ethanol solution. Based on the Q value, the regeneration performance of BC/ZIF-8 was higher than the carbon aerogel described by Sun et al. [19], nanocomposites synthesized by Zhang et al. [20], and polymers synthesized by Amin Abbasi et al. [72]. The persistent adsorption capacity of the BC/ZIF-8 is likely due to the structural stability of the ZIF-8 as indicated by the XRD, TGA and DTG analyses. From pH and adsorption strength perspectives, most of the B species are trigonal boric acid at pH = 6, but the bond strength

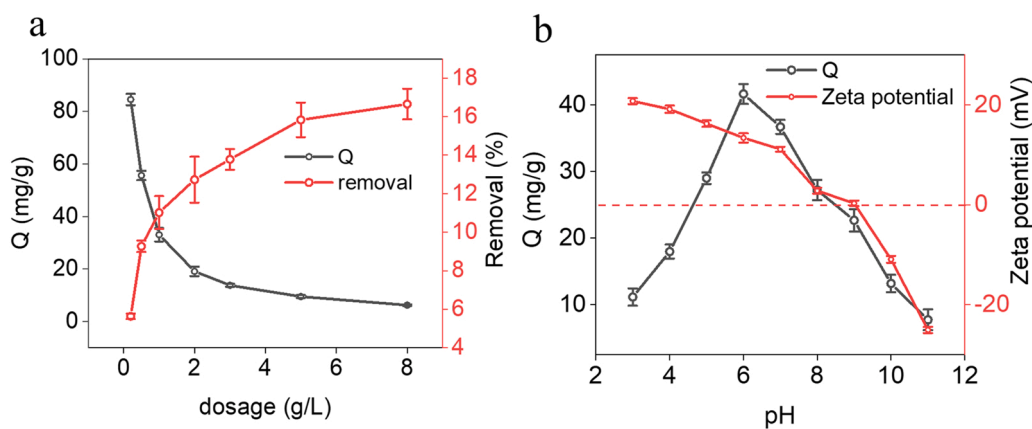**Fig. 7.** (a) Adsorption capacity and removal rate of B by BC/ZIF-8 with B concentrations ranging from 0.2 to 8.0 g L^{-1}. (b) Adsorption capacity at different initial pH values and relationship between zeta potential of BC/ZIF-8 and solution pH values.
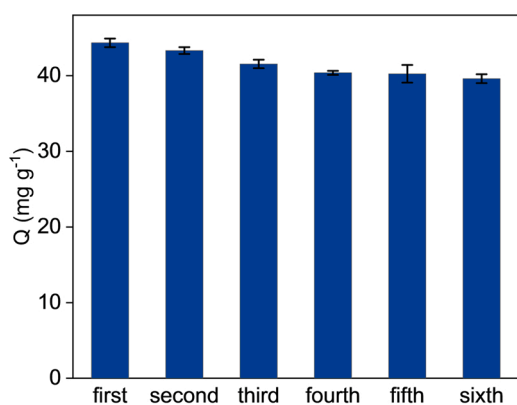

Fig. 9. The reacted BC/ZIF-8 was recovered and washed with NaOH/ethanol solution after each of the 6 desorption cycles. Error bars represent the standard deviation (n = 4).

between triangulated boric acid and hydroxyl groups is weak [73]. This weak bonding may lead to the high reuse capacity observed in our study.

3.4. Adsorption mechanisms

The adsorption performance of a material is related to its pore structure and surface functional groups. ZIF-8 has a diameter of ~11.6 Å and is formed by splicing six-membered rings (~3.4 Å) and four-membered rings. However, the four-membered ring is too restricted to allow guest molecules to pass through [74]. To evaluate the transport capacity of the two forms of boric acid to pass through the six-membered ring of ZIF-8, we calculated the size of trigonal boric acid ($H_3BO_3^0$) and tetrahedral boric acid ($B(OH)_4^-$) using the software Multiwfn [75]. We found that the pore size of tetrahedral boric acid anion $\approx$ 3.39 Å was smaller than the pore size of ZIF-8 (3.4 Å) [33] and the size of triangular boronic acid $\approx$ 3.4 Å was similar to that of ZIF-8. This pore size analysis suggests that trigonal boric acid and tetrahedral boric acid anion may diffuse directionally into the interior of ZIF-8 due to the pore size of ZIF-8 (conceptual model is presented in Fig. S2).

We further analyzed the FTIR spectra of BC, ZIF-8, BC/ZIF-8, and BC/ZIF-8-B to explore the mechanisms of B adsorption (Fig. 11a). Overall, the bands were similar among ZIF-8, BC/ZIF-8 and BC/ZIF-8-B, which were substantially different from BC. This indicated that the surface functional groups from the original BC were largely masked by in situ growth of ZIF-8 on the BC surface. The O-H asymmetric stretching vibrations at 3500 cm^{-1} were observed for all samples [76], which indicates the presence of hydroxyl groups (-OH) in BC, and the formation of Zn-OH due to the defects of Zn-O during the preparation of ZIF-8 [38, 77]. Compared with ZIF-8, the band intensity in the spectrum of BC/ZIF-8 was enhanced at 3500 cm^{-1}, suggesting BC may contribute additional hydroxyl groups for complexation. As shown in Fig. 12, solution aqueous species mainly exist in the form of trigonal boric acid under acidic conditions, and mainly exist in the form of tetrahedral boric acid under alkaline conditions. The -OH groups at the surface of BC and
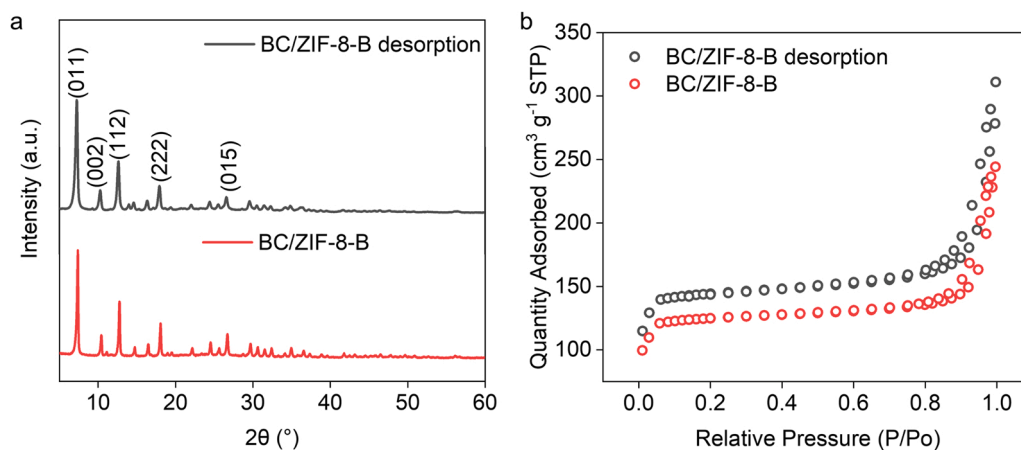

Fig. 10. (a) X-ray diffraction pattern of the sixth adsorption and desorption of BC/ZIF-8-B. (b) N$_2$ adsorption-desorption isotherms of the sixth adsorption and desorption of BC/ZIF-8-B.
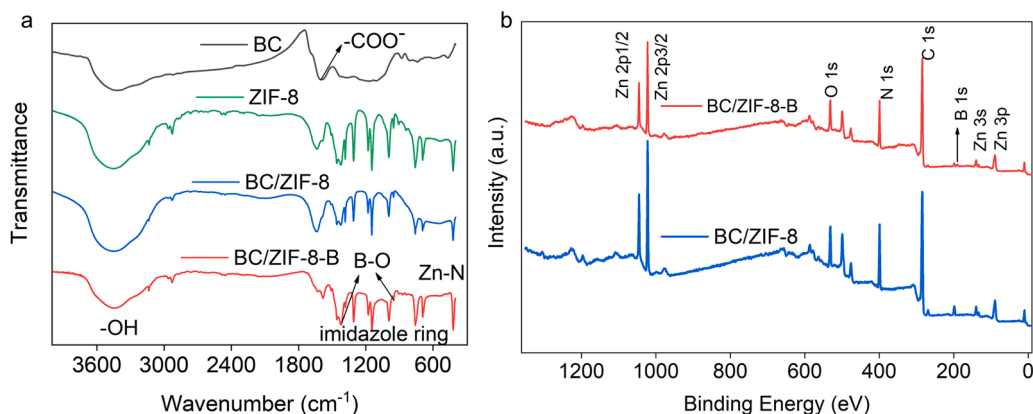
Fig. 11. (a) Fourier transform infrared spectra (FTIR) of BC (black), ZIF-8 (green), BC/ZIF-8 (blue) and BC/ZIF-8-B (red); (b) X-ray Photoelectron Spectrometry (XPS) wide scan spectra of BC/ZIF-8 (red) and BC/ZIF-8-B (blue).

Zn-OH on BC/ZIF-8 possibly account for B adsorption by forming monochelate, bichelate or tetradentate complexes under acidic conditions [78]. In addition, when pH<PZC, the surface of the nanocomposite is positively charged, which facilitates the binding of $B(OH)_4^-$ through electrostatic attraction. At low pH, $B(OH)_4^-$ may bond to the protonated ($-OH^{2+}$) surface of the BC/ZIF-8 by Lewis acid-base interactions, although $B(OH)_4^-$ is not the dominant aqueous species at low pH [79]. At high pH, by Lewis acid-base interactions, the electron-deficient aqueous species $H_3BO_3^0$ may bond to the deprotonated ($-O^-$) functional group at the surface of BC/ZIF-8, and increased concentrations of $B(OH)_4^-$ may also lead to the formation of Zn-O-B coordination with Zn(II) [79,80]. Notably, the concentration of $B(OH)_4^-$ is substantially higher at conditions where pH > PZC, which may cause its electrostatic repulsion from the negatively charged surface of BC/ZIF-8. At the experimental pH value (pH=6), trigonal boric acid accounts for about 99.94% and tetrahedral boric acid accounts for about 0.06% of the total aqueous species. Therefore, hydrogen bonding (-OH complexation) and electrostatic attraction may serve as fundamental forces in the adsorption of B by BC/ZIF-8. This is also reflected in FTIR, where intensity of the band at 3500 cm^{-1} in the BC/ZIF-8-B spectrum is reduced compared to BC/ZIF-8, likely caused by the formation of complexes between the hydroxyl groups (-OH) and $H_3BO_3^0$ and $B(OH)_4^-$ [81]. The band intensities at 950 cm^{-1} associated with asymmetric stretching of B-O in tetrahedral boric acid anions [82] and 1413 cm^{-1} associated with the asymmetric stretching of B-O in trigonal boric acid [78] were enhanced after B adsorption. This indicates that both trigonal and tetrahedral boric acids

were successfully adsorbed by BC/ZIF-8. In addition, bands associated with Zn-N at 416 cm^{-1} were consistently observed in the spectra of BC/ZIF-8 and BC/ZIF-8-B. Owing to the core structure of the ZIF-8, the zinc ion is linked to the N in 2-methylimidazole, the consistent presence of Zn-N indicates that the surface structure of the ZIF-8 is relatively stable [83].

Based on the XPS analyses (Fig. 11b), sub-peaks of each of the primary peaks in the wide scan spectra are presented in Fig. S1. The peaks at 1045 eV, 1022 eV, 531 eV, 398 eV, 285 eV, 139 eV and 89 eV correspond to Zn 2p1/2, Zn 2p3/2, O 1s, N 1s, C 1s, Zn 3s and Zn 3p, respectively [84]. In the C 1s spectrum, the sub-peak at 285.36 eV was likely associated with C=O from -COO$^-$ functional groups of BC, which is also confirmed in the FTIR spectra [44]. The sub-peaks at 398.78 eV and 399.56 eV in the N 1s spectrum were likely associated with C-N and C=N in 2-methylimidazole. A peak associated with B appeared at 190 eV after the composite captured B. After BC/ZIF-8 adsorbed B, the Zn 2p peak moved to higher binding energy, which indicates that Zn was involved in the adsorption reaction [85].

3.5. Adsorption of B in HF-FPW

We performed adsorption experiments on the B adsorption capacity of BC/ZIF-8 to investigate B removal capacity in a complex system. FPW has high ionic strength with various elements and organic constituents (full profiling is presented in Table 2). Of particular interest, the B concentration in the FPW is 42 mg L^{-1}. As shown in Fig. 13, the removal rate of B in FPW by BC/ZIF-8 is 18.36% (equilibrium adsorption capacity was 15.45 mg g^{-1}), which is 5.99% lower than the control group (pure B solution with a concentration of 42 mg L^{-1}). Compared with other inorganic materials such as Fe$_3$O$_4$ [21], MgO [22], fly ash [86] and ZIF-8 [87], the synthesized BC/ZIF-8 has the highest B removal efficiency.

The reduced B adsorption in FPW relative to the pure B solution is likely caused by ion competition for adsorption and elevated ionic strength [88]. For many minerals, elevated ionic strength may reduce the adsorption efficiency [89,90]. At pH = 6, the positively charged surface of BC/ZIF-8 and coexisting anions exerts some influence on the adsorption of B in BC/ZIF-8 through the electrostatic attraction [91]. Anions in FPW may form surface complexes with Zn in the BC/ZIF-8, in the same way that zinc ions and carbonates form Zn-O-C(O)- [65], and occupying Zn-OH hinders its formation with B to form Zn-O-B. The influence of organics in FPW may be limited due to their overall low concentrations (Table 2).
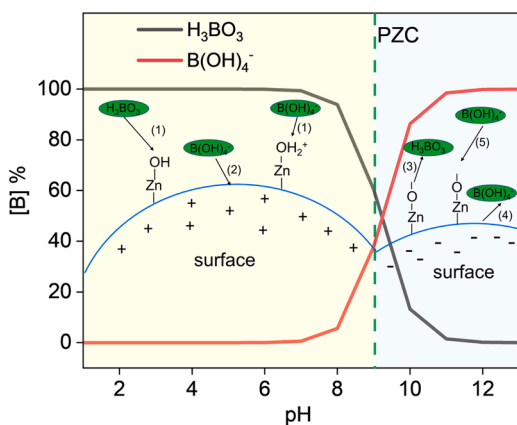
4. Conclusions

In this study, we synthesized BC/ZIF-8 and tested its ability to

Fig. 12. Conceptual model of the possible mechanisms of B adsorption by BC/ZIF-8, including (1) hydrogen bonding, (2) electrostatic attraction, (3) Lewis acid-base interactions, (4) electrostatic repulsion and (5) Zn-O-B coordination. The dissolved borate species are determined using Visual Minteq.

Table 2
Chemical composition of the tested hydraulic fracturing flowback and produced water.

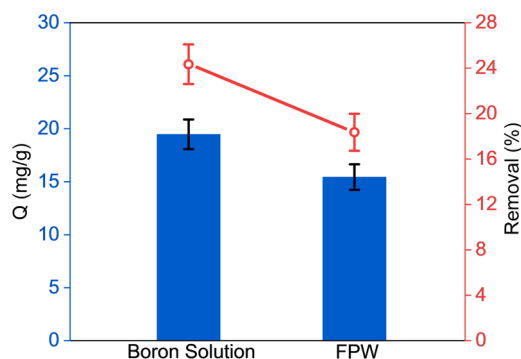| Element	K^+	Na^+	Mg^{2+}	Ca^{2+}	B	HCO_3^-	SO_4^{2-}	Cl^-	TOC	TN
Concentration (mg L^{-1})	226	8149	26	186	42	691	34	13049	58	58

Fig. 13. Comparison of adsorption properties of BC/ZIF-8 applied to the B solution and FPW.

remove B from water ($C_0 = 300$ mg L^{-1}) and FPW ($C_0 = 42$ mg L^{-1}). Results showed high B adsorption capacities in both clean (44 mg g^{-1}) and complex (FPW) solutions (15.45 mg g^{-1}). Compared to ZIF-8, the adsorption capacity for BC/ZIF-8 increased by 76%. The adsorption of B to BC/ZIF-8 was a spontaneous but endothermic process, and its kinetics were the best fit by a pseudo-first-order kinetics model and the Langmuir adsorption isotherm. Through six regeneration cycles, we demonstrated that BC/ZIF-8 has a good reuse capacity when applied for B adsorption. By comparison, the B removal rate in FPW was 5.99% lower than that of the control group (pure B solution at similar conditions) due to ion competition and the elevated ionic strength decreases the electric field around the charged particle surface. Physicochemical characterization showed that BC/ZIF-8 has a stable structure, suggesting that hydrogen bonding (-OH complexation) and electrostatic attraction are the fundamental forces in the binding of B to BC/ZIF-B. The BC/ZIF-8 composite allows for more sustainable use of wastes due to the reuse of waste biomass to produce BC, and shows the promise of broader industrial applications and water treatment using BC/ZIF-8.

CRediT authorship contribution statement

Mina Luo wrote the paper with inputs from all authors. Chunmei Zhu, Qingmei Chen, Fang Song conducted the experiments. Weiduo Hao, Zhengtao Shen, Kurt O. Konhauser, Daniel S. Alessi edited the paper. Cheng Zhong edited the paper and supervised the project.

Declaration of Competing Interest

The authors declare that they have no known competing financial interests or personal relationships that could have appeared to influence the work reported in this paper.

Data Availability

Data will be made available on request.

Acknowledgement

Appendix A. Supporting information

References

[1] Y. He, Estimation of fracture production and water breakthrough locations of multi-stage fractured horizontal wells combining pressure-transient analysis and electrical resistance tomography, J. Pet. Sci. Eng. 194 (2020), 107479, https://doi.org/10.1016/j.petrol.2020.107479.

[2] E.J. Folkerts, T.A. Blewett, P. Delompré, W.T. Mehler, S.L. Flynn, C. Sun, Y. Zhang, J.W. Martin, D.S. Alessi, G.G. Goss, Toxicity in aquatic model species exposed to a temporal series of three different flowback and produced water samples collected from a horizontal hydraulically fractured well, Ecotoxicol. Environ. Saf. 180 (2019) 600–609, https://doi.org/10.1016/j.ecoenv.2019.05.054.

[3] C. Zhong, J. Li, S.L. Flynn, C.L. Nesbø, C. Sun, K. von Gunten, B.D. Lanoil, G. G. Goss, J.W. Martin, D.S. Alessi, Temporal changes in microbial community composition and geochemistry in flowback and produced water from the duvernay formation, ACS Earth Space Chem. 3 (2019) 1047–1057, https://doi.org/10.1021/acsearthspacechem.9b00037.

[4] C. Zhong, C.L. Nesbø, G.G. Goss, B.D. Lanoil, D.S. Alessi, Response of aquatic microbial communities and bioindicator modelling of hydraulic fracturing flowback and produced water, FEMS Microbiol. Ecol. 96 (2020), https://doi.org/10.1093/femsec/fiaa068.

[5] C. Zhong, C.L. Nesbø, K. Gunten, Y. Zhang, X. Shao, R. Jin, K.O. Konhauser, G. G. Goss, J.W. Martin, Y. He, P. Qian, B.D. Lanoil, D.S. Alessi, Complex impacts of hydraulic fracturing return fluids on soil microbial community respiration, structure and functional potentials, Environ. Microbiol. 1462–2920 (2022) 16009, https://doi.org/10.1111/1462-2920.16009.

[6] R. Bondu, W. Kloppmann, M.O. Naumenko-Dèzes, P. Humez, B. Mayer, Potential impacts of shale gas development on inorganic groundwater chemistry: implications for environmental baseline assessment in shallow aquifers, Environ. Sci. Technol. 55 (2021) 9657–9671, https://doi.org/10.1021/acs.est.1c01172.

[7] Y. Kreisserman, S. Emmanuel, Release of particulate iron sulfide during shale-fluid interaction, Environ. Sci. Technol. 52 (2018) 638–643, https://doi.org/10.1021/acs.est.7b05350.

[8] N.N. Xia, H.Y. Zhang, Z.H. Hu, F. Kong, F. He, A functionalized bio-based material with abundant mesopores and catechol groups for efficient removal of boron, Chemosphere 263 (2021), 128202, https://doi.org/10.1016/j.chemosphere.2020.128202.

[9] N.J. Williams, P.A. Kelly, K.G. Berard, E.L. Dore', N.L. Emery, C.F. Williams, S. Mukhopadhyay, Fracturing Fluid With Low-Polymer Loading Using a New Set of Boron Crosslinkers: Laboratory and Field Studies, in: All Days, SPE, Lafayette, Louisiana, USA, 2012: p. SPE-151715-MS. https://doi.org/10.2118/151715-MS.

[10] H. Chang, T. Li, B. Liu, R.D. Vidic, M. Elimelech, J.C. Crittenden, Potential and implemented membrane-based technologies for the treatment and reuse of flowback and produced water from shale gas and oil plays: a review, Desalination 455 (2019) 34–57, https://doi.org/10.1016/j.desal.2019.01.001.

[11] E. Henry Ezechi, M.H. Isa, S.R.Mohamed Kutty, Boron in produced water: challenges and improvements: a comprehensive review, J. Appl. Sci. 12 (2012) 402–415, https://doi.org/10.3923/jas.2012.402.415.

[12] T. Bu, F. Chen, X. He, Y. Yang, W. Wang, Researching the complexing conditions of residual boron in produced water from oil & gas fields, Process Saf. Environ. Prot. 116 (2018) 254–261, https://doi.org/10.1016/j.psep.2018.02.013.

[13] E. Yoshikawa, A. Sasaki, M. Endo, Removal of boron from wastewater by the hydroxyapatite formation reaction using acceleration effect of ammonia, J. Hazard. Mater. 237– 238 (2012) 277–282, https://doi.org/10.1016/j.jhazmat.2012.08.045.

[14] N. Biçak, N. Bulutçu, B.F. Şenkal, M. Gazi, Modification of crosslinked glycidyl methacrylate-based polymers for boron-specific column extraction, React. Funct. Polym. 47 (2001) 175–184, https://doi.org/10.1016/S1381-5148(01)00025-6.

[15] L. Liu, X. Xie, S. Qi, R. Li, X. Zhang, X. Song, C. Gao, Thin film nanocomposite reverse osmosis membrane incorporated with UiO-66 nanoparticles for enhanced boron removal, J. Membr. Sci. 580 (2019) 101–109, https://doi.org/10.1016/j.memsci.2019.02.072.

[16] Q. Wu, M. Liu, X. Wang, A novel chitosan based adsorbent for boron separation, Sep. Purif. Technol. 211 (2019) 162–169, https://doi.org/10.1016/j.seppur.2018.09.070.

[17] M. Ruiz, C. Tobalina, H. Demey-Cedeño, J.A. Barron-Zambrano, A.M. Sastre, Sorption of boron on calcium alginate gel beads, React. Funct. Polym. 73 (2013) 653–657, https://doi.org/10.1016/j.reactfunctpolym.2013.01.014.

[18] J. Kluczka, M. Gnus, A. Kazek-Kęsik, G. Dudek, Zirconium-chitosan hydrogel beads for removal of boron from aqueous solutions, Polymer 150 (2018) 109–118, https://doi.org/10.1016/j.polymer.2018.07.010.

[19] L. Sun, J. Huang, H. Liu, Y. Zhang, X. Ye, H. Zhang, A. Wu, Z. Wu, Adsorption of boron by CA@KH-550@EPH@NMDG (CKEN) with biomass carbonaceous aerogels as substrate, J. Hazard. Mater. 358 (2018) 10–19, https://doi.org/10.1016/j.jhazmat.2018.06.040.

[20] T. Zhang, Y. Li, X. Zhao, W. Li, X. Sun, J. Li, R. Lu, A novel recyclable absorption material with boronate affinity, Sep. Purif. Technol. 272 (2021), 118880, https://doi.org/10.1016/j.seppur.2021.118880.

[21] T. Chen, Q. Wang, J. Lyu, P. Bai, X. Guo, Boron removal and reclamation by magnetic magnetite (Fe3O4) nanoparticle: an adsorption and isotopic separation study, Sep. Purif. Technol. 231 (2020), 115930, https://doi.org/10.1016/j.seppur.2019.115930.

[22] P. Li, C. Liu, L. Zhang, S. Zheng, Y. Zhang, Enhanced boron adsorption onto synthesized MgO nanosheets by ultrasonic method, Ultrason. Sonochem. 34 (2017) 938–946, https://doi.org/10.1016/j.ultsonch.2016.07.029.

[23] T. Kameda, J. Oba, T. Yoshioka, New treatment method for boron in aqueous solutions using Mg–Al layered double hydroxide: kinetics and equilibrium studies, J. Hazard. Mater. 293 (2015) 54–63, https://doi.org/10.1016/j.jhazmat.2015.03.015.

[24] Z. Wang, Z. Wu, Y. Zhang, J. Meng, Hyperbranched-polyol-tethered poly (amic acid) electrospun nanofiber membrane with ultrahigh adsorption capacity for boron removal, Appl. Surf. Sci. 402 (2017) 21–30, https://doi.org/10.1016/j.apsusc.2017.01.070.

[25] Y. Fang, J. Wen, G. Zeng, F. Jia, S. Zhang, Z. Peng, H. Zhang, Effect of mineralizing agents on the adsorption performance of metal–organic framework MIL-100(Fe) towards chromium(VI, Chem. Eng. J. 337 (2018) 532–540, https://doi.org/10.1016/j.cej.2017.12.136.

[26] H. Wang, W. Zhu, Y. Ping, C. Wang, N. Gao, X. Yin, C. Gu, D. Ding, C.J. Brinker, G. Li, Controlled fabrication of functional capsules based on the synergistic interaction between polyphenols and mofs under weak basic condition, ACS Appl. Mater. Interfaces 9 (2017) 14258–14264, https://doi.org/10.1021/acsami.7b01788.

[27] J. Wen, Y. Fang, G. Zeng, Progress and prospect of adsorptive removal of heavy metal ions from aqueous solution using metal–organic frameworks: a review of studies from the last decade, Chemosphere 201 (2018) 627–643, https://doi.org/10.1016/j.chemosphere.2018.03.047.

[28] O.K. Farha, I. Eryazici, N.C. Jeong, B.G. Hauser, C.E. Wilmer, A.A. Sarjeant, R. Q. Snurr, S.T. Nguyen, A.Ö. Yazaydın, J.T. Hupp, Metal–organic framework materials with ultrahigh surface areas: is the sky the limit, ?, J. Am. Chem. Soc. 134 (2012) 15016–15021, https://doi.org/10.1021/ja3055639.

[29] H.-P. Jing, C.-C. Wang, Y.-W. Zhang, P. Wang, R. Li, Photocatalytic degradation of methylene blue in ZIF-8, RSC Adv. 4 (2014) 54454–54462, https://doi.org/10.1039/C4RA08820D.

[30] H. Bux, F. Liang, Y. Li, J. Cravillon, M. Wiebcke, J. Caro, Zeolitic imidazolate framework membrane with molecular sieving properties by microwave-assisted solvothermal synthesis, J. Am. Chem. Soc. 131 (2009) 16000–16001, https://doi.org/10.1021/ja907359t.

[31] Z. Mo, D. Tai, H. Zhang, A. Shahab, A comprehensive review on the adsorption of heavy metals by zeolite imidazole framework (ZIF-8) based nanocomposite in water, Chem. Eng. J. 443 (2022) 136320, https://doi.org/10.1016/j.cej.2022.136320.

[32] D. Saliba, M. Ammar, M. Rammal, M. Al-Ghoul, M. Hmadeh, Crystal growth of ZIF-8, ZIF-67, and their mixed-metal derivatives, J. Am. Chem. Soc. 140 (2018) 1812–1823, https://doi.org/10.1021/jacs.7b11589.

[33] K.S. Park, Z. Ni, A.P. Côté, J.Y. Choi, R. Huang, F.J. Uribe-Romo, H.K. Chae, M. O'Keeffe, O.M. Yaghi, Exceptional chemical and thermal stability of zeolitic imidazolate frameworks, Proc. Natl. Acad. Sci. U. S. A. 103 (2006) 10186–10191, https://doi.org/10.1073/pnas.0602439103.

[34] J. Tang, R.R. Salunkhe, J. Liu, N.L. Torad, M. Imura, S. Furukawa, Y. Yamauchi, Thermal conversion of core–shell metal–organic frameworks: a new method for selectively functionalized nanoporous hybrid carbon, J. Am. Chem. Soc. 137 (2015) 1572–1580, https://doi.org/10.1021/ja511539a.

[35] X. Hu, J. Wen, H. Zhang, Q. Wang, C. Yan, L. Xing, Can epicatechin gallate increase Cr(VI) adsorption and reduction, Chem. Eng. J. 391 (2020), 123501, https://doi.org/10.1016/j.cej.2019.123501.

[36] Z. Veličković, G.D. Vuković, A.D. Marinković, M.-S. Moldovan, A.A. Perić-Grujić, P. S. Uskoković, M.Đ. Ristić, Adsorption of arsenate on iron(III) oxide coated ethylenediamine functionalized multiwall carbon nanotubes, Chem. Eng. J. 181–182 (2012) 174–181, https://doi.org/10.1016/j.cej.2011.11.052.

[37] N.L. Torad, M. Hu, Y. Kamachi, K. Takai, M. Imura, M. Naito, Y. Yamauchi, Facile synthesis of nanoporous carbons with controlled particle sizes by direct carbonization of monodispersed ZIF-8 crystals, Chem. Commun. 49 (2013) 2521, https://doi.org/10.1039/c3cc38955c.

[38] Y. Wang, W. Zhao, Z. Qi, L. Zhang, Y. Zhang, H. Huang, Y. Peng, Designing ZIF-8/ hydroxylated MWCNT nanocomposites for phosphate adsorption from water: capability and mechanism, Chem. Eng. J. 394 (2020), 124992, https://doi.org/10.1016/j.cej.2020.124992.

[39] J. Abdi, M. Vossoughi, N.M. Mahmoodi, I. Alemzadeh, Synthesis of metal-organic framework hybrid nanocomposites based on GO and CNT with high adsorption capacity for dye removal, Chem. Eng. J. 326 (2017) 1145–1158, https://doi.org/10.1016/j.cej.2017.06.054.

[40] R. Zhao, H. Liao, X. Wu, X. Cao, Selective adsorption behaviours of MOFs@SiO2 with different pore sizes and shell thicknesses, J. Solid State Chem. 292 (2020), 121693, https://doi.org/10.1016/j.jssc.2020.121693.

[41] F. Rezaei, S. Lawson, H. Hosseini, H. Thakkar, S. Hajari, S. Monjezi, A. A. Rownaghi, MOF-74 and UTSA-16 film growth on monolithic structures and their CO2 adsorption performance, Chem. Eng. J. 313 (2017) 1346–1353, https://doi.org/10.1016/j.cej.2016.11.058.

[42] Q.-L. Zhu, Q. Xu, Metal–organic framework composites, Chem. Soc. Rev. 43 (2014) 5468–5512, https://doi.org/10.1039/C3CS60472A.

[43] W.-J. Liu, H. Jiang, H.-Q. Yu, Development of biochar-based functional materials: toward a sustainable platform carbon material, Chem. Rev. 115 (2015) 12251–12285, https://doi.org/10.1021/acs.chemrev.5b00195.

[44] J.-H. Yuan, R.-K. Xu, H. Zhang, The forms of alkalis in the biochar produced from crop residues at different temperatures, Bioresour. Technol. 102 (2011) 3488–3497, https://doi.org/10.1016/j.biortech.2010.11.018.

[45] Y. Chun, G. Sheng, C.T. Chiou, B. Xing, Compositions and sorptive properties of crop residue-derived chars, Environ. Sci. Technol. 38 (2004) 4649–4655, https://doi.org/10.1021/es035034w.

[46] S. Kumar, R.E. Masto, L.C. Ram, P. Sarkar, J. George, V.A. Selvi, Biochar preparation from Parthenium hysterophorus and its potential use in soil application, Ecol. Eng. 55 (2013) 67–72, https://doi.org/10.1016/j.ecoleng.2013.02.011.

[47] A. Méndez, A. Gómez, J. Paz-Ferreiro, G. Gascó, Effects of sewage sludge biochar on plant metal availability after application to a Mediterranean soil, Chemosphere 89 (2012) 1354–1359, https://doi.org/10.1016/j.chemosphere.2012.05.092.

[48] R. Xu, S. Xiao, J. Yuan, A. Zhao, Adsorption of methyl violet from aqueous solutions by the biochars derived from crop residues, Bioresour. Technol. 102 (2011) 10293–10298, https://doi.org/10.1016/j.biortech.2011.08.089.

[49] J. Wang, S. Wang, Preparation, modification and environmental application of biochar: a review, J. Clean. Prod. 227 (2019) 1002–1022, https://doi.org/10.1016/j.jclepro.2019.04.282.

[50] J.D. Clogston, A.K. Patri, Zeta potential measurement, in: S.E. McNeil (Ed.), Characterization of Nanoparticles Intended for Drug Delivery, Humana Press, Totowa, NJ, 2011, pp. 63–70, https://doi.org/10.1007/978-1-60327-198-1_6.

[51] W. Tian, Q. Gao, Y. Tan, Z. Li, Unusual interconnected graphitized carbon nanosheets as the electrode of high-rate ionic liquid-based supercapacitor, Carbon 119 (2017) 287–295, https://doi.org/10.1016/j.carbon.2017.04.050.

[52] J. Ding, H. Wang, Z. Li, K. Cui, D. Karpuzov, X. Tan, A. Kohandehghan, D. Mitlin, Peanut shell hybrid sodium ion capacitor with extreme energy–power rivals lithium ion capacitors, Energy Environ. Sci. 8 (2015) 941–955, https://doi.org/10.1039/C4EE02986K.

[53] J. Luo, X. Li, C. Ge, K. Müller, H. Yu, P. Huang, J. Li, D.C.W. Tsang, N.S. Bolan, J. Rinklebe, H. Wang, Sorption of norfloxacin, sulfamerazine and oxytetracycline by KOH-modified biochar under single and ternary systems, Bioresour. Technol. 263 (2018) 385–392, https://doi.org/10.1016/j.biortech.2018.05.022.

[54] Q. Wang, Z. Lai, J. Mu, D. Chu, X. Zang, Converting industrial waste cork to biochar as Cu (II) adsorbent via slow pyrolysis, Waste Manag. 105 (2020) 102–109, https://doi.org/10.1016/j.wasman.2020.01.041.

[55] P. Zhu, J. Lin, L. Xie, M. Duan, D. Chen, D. Luo, Y. Wu, Visible light response photocatalytic performance of Z-scheme Ag 3 PO 4 /GO/UiO–66–NH 2 photocatalysts for the levofloxacin hydrochloride, Langmuir 37 (2021) 13309–13321, https://doi.org/10.1021/acs.langmuir.1c01901.

[56] M. Wu, L. Xia, Y. Li, D. Yin, J. Yu, W. Li, N. Wang, X. Li, J. Cui, W. Chu, Y. Cheng, M. Hu, Automated and remote synthesis of poly(ethylene glycol)-mineralized ZIF-8 composite particles via a synthesizer assisted by femtosecond laser micromachining, Chin. Chem. Lett. 33 (2022) 497–500, https://doi.org/10.1016/j.cclet.2021.07.004.

[57] H. Yang, R. Yan, H. Chen, D.H. Lee, C. Zheng, Characteristics of hemicellulose, cellulose and lignin pyrolysis, Fuel 86 (2007) 1781–1788, https://doi.org/10.1016/j.fuel.2006.12.013.

[58] L. Feng, K.-Y. Wang, G.S. Day, M.R. Ryder, H.-C. Zhou, Destruction of metal–organic frameworks: positive and negative aspects of stability and lability, Chem. Rev. 120 (2020) 13087–13133, https://doi.org/10.1021/acs.chemrev.0c00722.

[59] K. Weber, S. Eichenauer, E. Stadlbauer, M.-A. Schulten, T. Echterhof, C. Kammann, H.-P. Schmidt, A. Gerlach, H. Gerlach, Verwendung von Biomassekarbonisaten, in: P. Quicker, K. Weber (Eds.), Biokohle, Springer Fachmedien Wiesbaden, Wiesbaden, 2016, pp. 213–346, https://doi.org/10.1007/978-3-658-03689-8_5.

[60] P. Arabkhani, H. Javadian, A. Asfaram, M. Ateia, Decorating graphene oxide with zeolitic imidazolate framework (ZIF-8) and pseudo-boehmite offers ultra-high adsorption capacity of diclofenac in hospital effluents, Chemosphere 271 (2021), 129610, https://doi.org/10.1016/j.chemosphere.2021.129610.

[61] G.L. Long, J.D. Winefordner, Limit of detection. A closer look at the IUPAC definition, Anal. Chem. 55 (1983) 712A–724A, https://doi.org/10.1021/ac00258a001.

[62] P.A. Monson, Understanding adsorption/desorption hysteresis for fluids in mesoporous materials using simple molecular models and classical density functional theory, Microporous Mesoporous Mater. 160 (2012) 47–66, https://doi.org/10.1016/j.micromeso.2012.04.043.

[63] B. Li, L. Yang, C. Wang, Q. Zhang, Q. Liu, Y. Li, R. Xiao, Adsorption of Cd(II) from aqueous solutions by rape straw biochar derived from different modification processes, Chemosphere 175 (2017) 332–340, https://doi.org/10.1016/j.chemosphere.2017.02.061.

[64] Y. Li, H. Zhu, C. Zhang, M. Cheng, H. He, PEI-grafted magnetic cellulose for Cr(VI) removal from aqueous solution, Cellulose 25 (2018) 4757–4769, https://doi.org/10.1007/s10570-018-1868-2.

[65] M. Jian, B. Liu, G. Zhang, R. Liu, X. Zhang, Adsorptive removal of arsenic from aqueous solution by zeolitic imidazole framework-8 (ZIF-8) nanoparticles, Colloids Surf. A: Physicochem. Eng. Asp. 465 (2015) 67–76, https://doi.org/10.1016/j.colsurfa.2014.10.023.

[66] M. Doğan, M. Alkan, Adsorption kinetics of methyl violet onto perlite, Chemosphere 50 (2003) 517–528, https://doi.org/10.1016/S0045-6535(02)00629-X.

[67] W. Plazinski, W. Rudzinski, A. Plazinska, Theoretical models of sorption kinetics including a surface reaction mechanism: a review, Adv. Colloid Interface Sci. 152 (2009) 2–13, https://doi.org/10.1016/j.cis.2009.07.009.

[68] X. Zhang, Y. Li, M. Wu, Y. Pang, Z. Hao, M. Hu, R. Qiu, Z. Chen, Enhanced adsorption of tetracycline by an iron and manganese oxides loaded biochar: kinetics, mechanism and column adsorption, Bioresour. Technol. 320 (2021), 124264, https://doi.org/10.1016/j.biortech.2020.124264.

[69] N.M. Mahmoodi, F. Najafi, A. Neshat, Poly (amidoamine-co-acrylic acid) copolymer: synthesis, characterization and dye removal ability, Ind. Crops Prod. 42 (2013) 119–125, https://doi.org/10.1016/j.indcrop.2012.05.025.

[70] M. Zhang, Y. Liu, T. Li, W. Xu, B. Zheng, X. Tan, H. Wang, Y. Guo, F. Guo, S. Wang, Chitosan modification of magnetic biochar produced from Eichhornia crassipes for enhanced sorption of Cr(vi) from aqueous solution, RSC Adv. 5 (2015) 46955–46964, https://doi.org/10.1039/C5RA02388B.

[71] C. Bai, L. Wang, Z. Zhu, Adsorption of Cr(III) and Pb(II) by graphene oxide/alginate hydrogel membrane: characterization, adsorption kinetics, isotherm and thermodynamics studies, Int. J. Biol. Macromol. 147 (2020) 898–910, https://doi.org/10.1016/j.ijbiomac.2019.09.249.

[72] A. Abbasi, W.Z.N. Yahya, M.M. Nasef, M. Moniruzzaman, A.S.M. Ghumman, H.K. Afolabi, Boron removal by glucamine-functionalized inverse vulcanized sulfur polymer, React. Funct. Polym. 177 (2022), 105311, https://doi.org/10.1016/j.reactfunctpolym.2022.105311.

[73] H. Ito, Y. Kono, A. Machida, Y. Mitsumoto, K. Omori, N. Nakamura, Y. Kondo, K. Ishihara, Kinetic study of the complex formation of boric and boronic acids with mono- and diprotonated ligands, Inorg. Chim. Acta 344 (2003) 28–36, https://doi.org/10.1016/S0020-1693(02)01268-9.

[74] D.F. Sava, M.A. Rodriguez, K.W. Chapman, P.J. Chupas, J.A. Greathouse, P.S. Crozier, T.M. Nenoff, Capture of volatile iodine, a gaseous fission product, by zeolitic imidazolate framework-8, J. Am. Chem. Soc. 133 (2011) 12398–12401, https://doi.org/10.1021/ja204757x.

[75] T. Lu, F. Chen, Multiwfn: a multifunctional wavefunction analyzer, J. Comput. Chem. 33 (2012) 580–592, https://doi.org/10.1002/jcc.22885.

[76] D. OzCimen, A. Ersoy-MeriCboyu, Characterization of biochar and bio-oil samples obtained from carbonization of various biomass materials, Renew. Energy 35 (2010) 1319–1324, https://doi.org/10.1016/j.renene.2009.11.042.

[77] M. Hu, Y. Ju, K. Liang, T. Suma, J. Cui, F. Caruso, Void engineering in metal–organic frameworks via synergistic etching and surface functionalization, Adv. Funct. Mater. 26 (2016) 5827–5834, https://doi.org/10.1002/adfm.201601193.

[78] J. Kamcev, M.K. Taylor, D. Shin, N.N. Jarenwattananon, K.A. Colwell, J.R. Long, Functionalized porous aromatic frameworks as high-performance adsorbents for the rapid removal of boric acid from water, Adv. Mater. 31 (2019), 1808027, https://doi.org/10.1002/adma.201808027.

[79] Y. Li, B. Gao, T. Wu, D. Sun, X. Li, B. Wang, F. Lu, Hexavalent chromium removal from aqueous solution by adsorption on aluminum magnesium mixed hydroxide, Water Res. 43 (2009) 3067–3075, https://doi.org/10.1016/j.watres.2009.04.008.

[80] M. Tan, W. Zhang, C. Fan, L. Li, H. Chen, R. Li, T. Luo, S. Han, Boric acid–catalyzed hard carbon microfiber derived from cotton as a high-performance anode for lithium-ion batteries, Energy Technol. 7 (2019), 1801164, https://doi.org/10.1002/ente.201801164.

[81] S. Bhagyaraj, M.A. Al-Ghouti, P. Kasak, I. Krupa, An updated review on boron removal from water through adsorption processes, Emergent Mater. 4 (2021) 1167–1186, https://doi.org/10.1007/s42247-021-00197-3.

[82] D. Peak, G.W. Luther, D.L. Sparks, ATR-FTIR spectroscopic studies of boric acid adsorption on hydrous ferric oxide, Geochim. Et. Cosmochim. Acta 67 (2003) 2551–2560, https://doi.org/10.1016/S0016-7037(03)00096-6.

[83] H. Zhang, M. Zhao, Y. Yang, Y.S. Lin, Hydrolysis and condensation of ZIF-8 in water, Microporous Mesoporous Mater. 288 (2019), 109568, https://doi.org/10.1016/j.micromeso.2019.109568.

[84] M. Chin, C. Cisneros, S.M. Araiza, K.M. Vargas, K.M. Ishihara, F. Tian, Rhodamine B degradation by nanosized zeolitic imidazolate framework-8 (ZIF-8, RSC Adv. 8 (2018) 26987–26997, https://doi.org/10.1039/C8RA03459A.

[85] Z. Li, S. Deng, G. Yu, J. Huang, V.C. Lim, As(V) and As(III) removal from water by a Ce–Ti oxide adsorbent: behavior and mechanism, Chem. Eng. J. 161 (2010) 106–113, https://doi.org/10.1016/j.cej.2010.04.039.

[86] N. Ozturk, D. Kavak, Adsorption of boron from aqueous solutions using fly ash: Batch and column studies, J. Hazard. Mater. 127 (2005) 81–88, https://doi.org/10.1016/j.jhazmat.2005.06.026.

[87] J. Lyu, N. Zhang, H. Liu, Z. Zeng, J. Zhang, P. Bai, X. Guo, Adsorptive removal of boron by zeolitic imidazolate framework: kinetics, isotherms, thermodynamics, mechanism and recycling, Sep. Purif. Technol. 187 (2017) 67–75, https://doi.org/10.1016/j.seppur.2017.05.059.

[88] L.-L. Li, X.-Q. Feng, R.-P. Han, S.-Q. Zang, G. Yang, Cr(VI) removal via anion exchange on a silver-triazolate MOF, J. Hazard. Mater. 321 (2017) 622–628, https://doi.org/10.1016/j.jhazmat.2016.09.029.

[89] W. Hao, K. Mänd, Y. Li, D.S. Alessi, P. Somelar, M. Moussavou, A.E. Romashkin, A. Lepland, K. Kirsimäe, N.J. Planavsky, K.O. Konhauser, The kaolinite shuttle links the Great Oxidation and Lomagundi events, Nat. Commun. 12 (2021) 2944, https://doi.org/10.1038/s41467-021-23304-8.

[90] W. Hao, S.L. Flynn, T. Kashiwabara, M.S. Alam, S. Bandara, L. Swaren, L.J. Robbins, D.S. Alessi, K.O. Konhauser, The impact of ionic strength on the proton reactivity of clay minerals, Chem. Geol. 529 (2019), 119294, https://doi.org/10.1016/j.chemgeo.2019.119294.

[91] J. Wen, X. Hu, Metal selectivity and effects of co-existing ions on the removal of Cd, Cu, Ni, and Cr by ZIF-8-EGCG nanoparticles, J. Colloid Interface Sci. 589 (2021) 578–586, https://doi.org/10.1016/j.jcis.2021.01.021.